Limits on Arcminute Scale Cosmic Microwave Background Anisotropy with the BIMA Array

W.L. Holzapfel[1], J.E. Carlstrom[2], L. Grego[3],
G. Holder[2], M. Joy[4], and E.D. Reese[2]

ABSTRACT

We have used the Berkeley-Illinois-Maryland-Association (BIMA) millimeter array outfitted with sensitive cm-wave receivers to search for Cosmic Microwave Background (CMB) anisotropies on arcminute scales. The interferometer was placed in a compact configuration which produces high brightness sensitivity, while providing discrimination against point sources. Operating at a frequency of 28.5 GHz, the *fwhm* primary beam of the instrument is $\sim 6.6'$. We have made sensitive images of seven fields, five of which where chosen specifically to have low IR dust contrast and be free of bright radio sources. Additional observations with the Owens Valley Radio Observatory (OVRO) millimeter array were used to assist in the location and removal of radio point sources. Applying a Bayesian analysis to the raw visibility data, we place limits on CMB anisotropy flat-band power $Q_{flat} = 5.6^{+3.0}_{-5.6}\,\mu$K and $Q_{flat} < 14.1\,\mu$K at 68% and 95% confidence. The sensitivity of this experiment to flat band power peaks at a multipole of $\ell = 5470$ which corresponds to an angular scale of $\sim 2'$. The most likely value of Q_{flat} is similar to the level of the expected secondary anisotropies.

Subject headings: cosmology: observation – cosmic microwave background

[1]Department of Physics, University of California, Berkeley CA 94720

[2]Department of Astronomy and Astrophysics, University of Chicago, Chicago IL 60637

[3]Harvard-Smithsonian Center for Astrophysics, Mail Stop 83, 60 Gardeen St., Cambridge MA 02138

[4]Space Science Laboratory, SD50, NASA Marshall Space Flight Center, Huntsville AL 35812

1. Introduction

The Cosmic Microwave Background (CMB) has the potential to be a powerful probe of the early universe. In the standard inflationary model, the CMB is imprinted with anisotropies that reflect the distribution of matter at the epoch of recombination. Observations of the CMB at degree angular scales probe structures which have recently collapsed at this epoch and for which the distribution of anisotropies is extremely sensitive to the cosmological model. On scales smaller than a few arcminutes, photon diffusion and the finite time of recombination damp the primordial fluctuations to near zero amplitude (Hu & White 1997). However, the subsequent reionization of the universe can create a host of secondary anisotropies of the CMB. For a review of the subject see Haiman & Knox (1999). On arcminute scales, secondary anisotropies generated since recombination are likely to dominate the primary signal.

There have been many previous searches for anisotropy in the CMB on arcminute scales; both interferometric and single dish techniques have been used successfully. In this paper we describe a search for arcminute-scale CMB anisotropies with the Berkeley Illinois Maryland Association (BIMA) interferometer in a compact configuration at 28.5 GHz. We begin with a discussion of the instrument, field selection and observations in §2. In §3, initial data reduction is described including point source detection and measurement. The Bayesian maximum likelihood analysis we apply to the data is described in §4. The results of applying this formalism to our data are presented in §5 including a discussion of the effects of point source subtraction. In §6, we discuss the levels of the expected signals. We summarize the previous work in this field in §7. Finally, in §8, we summarize the results and discuss prospects for future observations.

2. Instrument & Observations

The advent of low-noise, broad-band, millimeter-wave amplifiers has made interferometry a particularly attractive technique for detecting and imaging low contrast emission, such as anisotropy in the CMB. An interferometer directly samples the Fourier transform of the intensity distribution on the sky. By transforming the interferometer output, images of the sky are obtained which include angular scales determined by the size and spacing of the individual array elements. In this section, we describe the BIMA instrument, the selection of the fields, and their observation.

2.1. Instrument

The anisotropy observations described here were made with nine elements of the BIMA array outfitted with sensitive cm-wavelength receivers. The BIMA antennae are 6.1 m in diameter and produce $6.6'$ beams at 28.5 GHz. The receivers are based on low noise HEMT amplifiers (Pospieszalski et al. 1998) and are configured to respond only to right circularly polarized radiation. At the operating frequency of 28.5 GHz, the receiver noise temperatures range from $13 - 18$ K and the system temperatures were typically $35 - 55$ K depending on source elevation. The signals from the individual array elements are combined in the BIMA 2-bit digital correlator which was configured for these observations with 8 contiguous 100 MHz sections of 32 channels each. The array elements were placed in a compact 2-dimensional configuration which provides high brightness sensitivity as well as sufficient resolution to identify radio point sources.

We have also made supporting observations with the Owens Valley Radio Observatory (OVRO) array outfitted with the same cm-wave receivers. These observations were used primarily for locating and measuring point sources in the observed fields. The OVRO antennae are 10.4 m in diameter and produce $3.8'$ beams at 28.5 GHz. For a description of the instrument see Carlstrom et al. (1996). The BIMA and OVRO arrays, outfitted with cm-wavelength receivers, have been used to image more than 20 clusters (Carlstrom et al. 1999.

2.2. Field Selection

In this paper, we report the results of a search for CMB anisotropy in seven independent fields. Two of the fields, PC1643+46 and VLA1312+32, are centered at previously reported microwave decrements (Jones et al. 1997; Richards et al. 1997). In a companion paper (Holzapfel et al. 1999), we demonstrate that our data are inconsistent with models used to describe the claimed decrements. In 1997, we observed a third field in the direction of the quasar PSS0030+17 which was originally selected as a distant cluster candidate. The quasar is at redshift $z = 4.32$ and has two Ly α break galaxies within $10''$ (Djorgovski 1997). The way these three fields were selected would prevent us from

claiming that they could produce an unbiased measurement of CMB anisotropy. However, for the purpose of placing upper limits on CMB anisotropy, we are justified in making use of these observations.

In 1998, four additional fields were selected to be evenly distributed in right ascension and at convenient declinations for observations with the BIMA array. The fields were chosen to be in regions of low dust emission and contrast as determined from examination of IRAS 100 μm maps. The VLA NVSS (Condon et al. 1998) and FIRST (White et al. 1997) surveys were then used to select regions free of bright point sources at 1.4 GHz. Finally, we used the SkyView[5] Digitized sky survey and ROSAT WFC maps to check for bright optical or x-ray emission which could complicate follow-up observations. The pointing centers for each of the 7 fields are given in Table 1.

For one of the new fields, we used the OVRO array to check for radio sources at 28.5 GHz before beginning observations with the BIMA array. With a 7 pointing mosaic, we reached a map *rms* flux of $\sim 120\,\mu$Jy over a $8'$ region containing the entire BF0028+28 field observed with BIMA. We discovered a single source with a flux of 1.4 mJy. This and all fluxes in this paper have been corrected for the attenuation of the primary beam unless otherwise specified. The pointing center for the BIMA observations was chosen so that this source lied outside the observed field of view. Unfortunately, we did not have time to image all the observed fields with the OVRO array and it is possible that some of the fields observed in 1998 suffer from low level point source contamination.

2.3. BIMA Observations

All observations were made during the summers of 1997 and 1998, interspersed between observations of the Sunyaev-Zel'dovich effect (SZE) in x-ray selected clusters. In 1998, we selected four fields spaced in right ascension so that at any given time one of them had a hour angle suitable for observation. Each 20 minute source observation was bracketed by the observation of a calibration source. Including the time for calibration cycles, the fraction of time spent on source was $\sim 60\%$. The integration times for each of the 7 fields are given in Table 1. The fluxes of the calibration sources are all referenced to the flux of Mars which is uncertain by approximately 4% (see discussion in Grego 1998).

[5]We acknowledge the use of NASA's SkyView facility (http://skyview.gsfc.nasa.gov) located at NASA Goddard Space Flight Center.

3. Editing and Inspection

The data are edited using several criteria to ensure the integrity of the calibration and that the results remain free of systematics. It is possible for the beam of one dish to be obscured by one of its neighbors in the array. Baselines involving telescopes within 3% of the shadowing limit are discarded. The spectral channels are inspected for any interference and removed if they are believed to be contaminated. Low signal to noise channels near the edges of the correlated bandwidth are not used. The effective noise bandwidth of the correlator after accounting for the 2-bit digitization and removed end channels is ~ 540 MHz. Records with spurious system temperatures, caused by failed or aborted calibration cycles are discarded. Source data not bracketed by successful calibration cycles are discarded. During periods of poor weather, the phase coherence of the calibration sources becomes poor. All data that are bracketed by calibration cycles with poor phase coherence are also discarded.

3.1. Point Sources

Each data set is transformed to create a map with the DIFMAP package (Shepard, Pearson, & Taylor 1994). The maps are then searched for statistically significant unresolved emission. In order to remain unbiased in our search for point sources, we limit ourselves to the range of baselines greater than 2.4 kλ ($\ell > 15000$), which are completely independent of the baselines used in the anisotropy analysis. That way, we can be assured that the anisotropy results will not systematically depend on the point source detection and subtraction. In general, we find the flux and positions of the sources by fitting the Fourier transform of source model directly to the visibility data. The source model is multiplied by the measured primary beam response to take the attenuation of the source into account. In Table 2, we list the positions and fluxes of the significant point sources in the observed fields.

The brightest point source discovered was centered at $\alpha = 00^{\rm h}\,30^{\rm m}\,37.0^{\rm s}$, $\delta = +17^\circ\,05'\,12''$ (J2000), offset from the pointing center of the PSS0030+17 field by $\Delta\alpha = +294''$ and $\Delta\delta = +152''$. The observed flux is attenuated by the finite size of the array element beams which are measured to have a *fwhm* of $\sim 396''$.

Field Positions and Observation Times

Fields	α (J2000)	δ (J2000)	Observation Year(s)	Time (Hours)
PC1643+46	$16^{\rm h}\,45^{\rm m}\,11.3^{\rm s}$	$+46^\circ\,24'\,56''$	1997, 1998	43.1
VLA1312+32	$13^{\rm h}\,12^{\rm m}\,17.4^{\rm s}$	$+42^\circ\,38'\,05''$	1997	35.5
PSS0030+17	$00^{\rm h}\,30^{\rm m}\,16.4^{\rm s}$	$+17^\circ\,02'\,40''$	1997	36.6
BF0028+28	$00^{\rm h}\,28^{\rm m}\,04.4^{\rm s}$	$+28^\circ\,23'\,06''$	1998	77.6
HDF1236+62	$12^{\rm h}\,36^{\rm m}\,49.4^{\rm s}$	$+62^\circ\,12'\,58''$	1998	32.0
BF1821+59	$18^{\rm h}\,21^{\rm m}\,00.0^{\rm s}$	$+59^\circ\,15'\,00''$	1998	43.5
BF0658+55	$06^{\rm h}\,58^{\rm m}\,45.0^{\rm s}$	$+55^\circ\,17'\,00''$	1998	44.7

Table 1: Coordinates of the observed fields, years of observation, and cumulative time on source.

Subtracted Point Sources

		Positions (J2000)		From Map Center		
Field	Source	α	δ	$\Delta\alpha$	$\Delta\delta$	Flux (μJy)
PSS0030+17	–	$00^{\rm h}\,30^{\rm m}\,37.0^{\rm s}$	$+17^\circ\,05'\,12''$	294	152	12800 ± 1600
HDF1236+62	–	$12^{\rm h}\,36^{\rm m}\,44.4^{\rm s}$	$+62^\circ\,11'\,33''$	−34	−85	347 ± 59
PC1643+46	S_1'	$16^{\rm h}\,45^{\rm m}\,21.1^{\rm s}$	$+46^\circ\,25'\,46''$	102	50	227 ± 70
PC1643+46	S_2'	$16^{\rm h}\,45^{\rm m}\,12.2^{\rm s}$	$+46^\circ\,24'\,08''$	9	−48	113 ± 62
PC1643+46	S_3'	$16^{\rm h}\,45^{\rm m}\,22.7^{\rm s}$	$+46^\circ\,24'\,17''$	118	−40	237 ± 72
PC1643+46	S_1	$16^{\rm h}\,45^{\rm m}\,20.9^{\rm s}$	$+46^\circ\,25'\,43''$	100	47	227 ± 63
PC1643+46	S_2	$16^{\rm h}\,45^{\rm m}\,12.5^{\rm s}$	$+46^\circ\,24'\,13''$	6	−43	222 ± 63
PC1643+46	S_3	$16^{\rm h}\,45^{\rm m}\,23.0^{\rm s}$	$+46^\circ\,24'\,21''$	115	−36	262 ± 71

Table 2: Coordinates, distances from the anisotropy map center, and intrinsic fluxes of the significant sources in the field at 28.5 GHz. For PC1643+46, we first show the results when the positions of the sources (primed) are fixed and second when the positions are allowed to assume their best fit values.

This source is far from the center of the map and has an observed flux of 1.5 mJy. Correcting for the primary beam response, the intrinsic source flux is determined to be 12.8 ± 1.6 mJy.

A significant point source was detected in deep observations of the HDF1236+62 field with both the OVRO and BIMA arrays. There were two pointings of the OVRO array with one centered on the position of the suspected point source. We simultaneously fit the raw OVRO and BIMA visibility data with a single component point source model. The source is the brightest in the observed field with a flux of $345 \pm 59\,\mu$Jy. It was centered at $\alpha = 12^{\rm h}\,36^{\rm m}\,44.4^{\rm s}$, $\delta = +62^\circ\,11'\,33''$ (J2000), offset from the BIMA pointing center by $\Delta\alpha = -34''$ and $\Delta\delta = -85''$. This source has the same position as the brightest source found in a deep radio image of the HDF at 8.4 GHz (Richards et al. 1998).

The field PC1643+46 was previously imaged with the Ryle telescope at 15 GHz (Jones et al. 1997). Three point sources were found in the observed field. In addition to our observations with the BIMA array, we have also imaged this same region with three pointings of the OVRO array operating at 28.5 GHz. Each of the three pointings were chosen to place the map center near one of the suspected point sources. The field observed with BIMA was imaged with *rms* flux density ranging from $40 - 100\,\mu{\rm Jy\,beam^{-1}}$. We have performed a simultaneous fit to the BIMA and OVRO visibility data in order to determine the positions and fluxes of the sources at 28.5 GHz. We have determined the fluxes of the sources using two different methods. First we fixed the positions of the sources to the positions found with the Ryle observations and solved for the three source fluxes. Introducing these three free parameters decreased the χ^2 of the fit to the visibility data by 25; this indi-

cates that the field suffers significant contamination from these sources. The uncertainties for the source fluxes, shown in Table 2, correspond to the change in flux which results in a increase in χ^2 of one while the other free parameters (two other fluxes) are allowed to assume their best fit values.

We repeated this analysis allowing the source positions as well as fluxes to vary. This procedure allows for differences in the positions determined by the BIMA and OVRO analysis and those of Jones et al. (1997). By allowing the positions to vary, and adding 6 new free parameters to the model, the χ^2 of the fit is reduced by 14 from the case where the source positions are fixed to the Ryle positions. Therefore, the differences from the Ryle positions are significant and in the rest of this work we adopt these new source positions. The differences between each of the new positions and those of Jones et al. (1997) are less than $6''$. When the uncertainties in the Ryle positions and those found here are taken into account, the positions determined by the two experiments are found to be consistent. The errors for each of the point source fluxes correspond to the change in flux required to produce to a change in χ^2 of one while the free paramenters (flux of the other two sources and the positions of all three sources) are allowed to assume their best fit values. In Table 2, we list the measured positions and fluxes of all the detected sources. These sources are removed from the raw data by taking the Fourier transform of the point source model modulated by the primary beam response and subtracting it directly from the visibility data.

3.2. Image Statistics

We have produced and analyzed images for each of the observed fields. The results for the long baseline data used in point source subtraction are listed in Table 3. We limit the data to baselines $> 2.4\,\mathrm{k}\lambda$ to guarantee that the data used to determine the point source fluxes and positions are completely independent of the anisotropy data. The *rms* for all the data is considerably lower. The map *rms* indicates the accuracy with which the flux of point sources can be measured with this subset of the BIMA data. For the fields PC1643+46 and HDF1236+62 the point source sensitivity is considerably better than listed here due to the supporting OVRO observations. The results using only the short baselines used in the anisotropy analysis are listed in Table 4. For the short baseline maps, we also express our results in terms of the *rms* Rayleigh-Jeans (RJ) temperature fluctuations. For both the short and long baseline maps, the observed *rms* values are compared to those expected from the noise properties of the visibilities. For the short baseline results, there are approximately ten independent beams in each observed field. If we assume that the map values are dominated by Gaussian distributed noise, the measured *rms* should be the same as the estimated value within approximately 10% at 68% confidence.

4. Analysis

Several recent papers have dealt with the analysis of CMB data from interferometers (Martin & Partridge 1988; Subrahmanyan et al. 1998; Hobson, Lasenby & Jones 1995; Hobson & Mageuijo 1996; Partridge et al. 1997; White et al. 1999). In this work, we follow the formalism presented in White et al. (1998) for the Bayesian analysis of CMB data.

In theories which predict Gaussian temperature fluctuations, the fundamental theoretical construct is the correlation matrix of the measured data. Since the data are the visibilities measured at a set of points $\mathbf{u}_i$, we will need to know the correlation matrices for the signal and noise of the observed visibilities. The measured fluxes are given by

$$V(\mathbf{u}) = \frac{\partial B_\nu}{\partial T} \int d\mathbf{x}\ \Delta T(\mathbf{x})\ A(\mathbf{x}) e^{2\pi i \mathbf{u}\cdot\mathbf{x}} \quad , \qquad (1)$$

where $\Delta T(\mathbf{x})$ is the temperature distribution on the sky, $A(\mathbf{x})$ is the primary beam of the telescope,

$$\frac{\partial B_\nu}{\partial T} = 2k_B \left(\frac{k_B T}{hc}\right)^2 \frac{x^4 e^x}{(e^x-1)^2} \quad , \qquad (2)$$

k_B is Boltzmann's constant, and $x \equiv h\nu/k_B T_{\mathrm{cmb}}$. We define the visibility correlation matrix,

$$\begin{aligned} C_{ij}^V &\equiv \langle V^*(\mathbf{u}_i) V(\mathbf{u}_j)\rangle \\ &= \left(\frac{\partial B_\nu}{\partial T}\right)^2 \int_0^\infty w\, dw\ S(w) W_{ij}(w)\,, \end{aligned} \qquad (3)$$

which is proportional to the product of the power spectrum, $S(w)$, and the visibility window function. The window function is given by

$$W_{ij}(|\mathbf{w}|) \equiv \int_0^{2\pi} d\theta_w\ \widetilde{A}^*(\mathbf{u}_i - \mathbf{w}) \widetilde{A}(\mathbf{u}_j - \mathbf{w}) \quad , \qquad (4)$$

where $\widetilde{A}(\mathbf{u})$ is the Fourier transform of the telescope primary beam. In the case of a single flat band power

Image Analysis for Baselines $> 2.4\,\mathrm{k}\lambda$

Field	beamsize($''$)	*rms* (μJy beam^{-1})	
		estimated	measured
PC 1643+46	18.9×25.0	132	139
VLA 1312+32	18.8×26.0	134	122
PSS 0030+17	18.1×25.2	155	150
BF 0028+28	21.2×21.6	136	127
HDF 1236+62	22.5×23.9	195	207
BF 1821+59	21.7×23.6	152	160
BF 0658+55	21.6×23.2	158	157

Table 3: Image statistics for maps created using only the long baselines used to measure point sources. Columns 3 & 4 list the estimated and observed map *rms*.

Image Analysis for u-v Range $0.63 - 1.2\,\mathrm{k}\lambda$

Field	beamsize($''$)	*rms* (μJy beam^{-1})		*rms* (μK)	
		estimated	measured	estimated	measured
PC 1643+46	98.3×116.1	187	191	24.6	25.1
VLA 1312+32	95.2×113.4	225	223	31.3	31.0
PSS 0030+17	99.1×115.5	202	203	26.5	26.6
BF 0028+28	108.9×118.8	127	99	14.7	11.5
HDF 1236+62	110.9×122.0	206	168	22.8	18.6
BF 1821+59	108.4×122.4	174	224	19.7	22.4
BF 0658+55	105.2×148.0	252	304	24.3	29.3

Table 4: Image statistics for maps created using only the short baselines used in the anisotropy analysis. Columns 5 & 6 give the image results in *rms* RJ map temperature.

and $\ell > 60$, we can write

$$C_{ij}^V = \frac{6}{5\pi}\left(\frac{\partial B_\nu}{\partial T}\right)^2 Q_{flat}^2 \int_0^\infty \frac{dw}{w} W_{ij}(w) \quad , \qquad (5)$$

where

$$Q_{flat}^2 \equiv \frac{5}{24\pi} C_\ell \ell(\ell+1) \qquad (6)$$

is the normalization of the power spectrum. The correlation function of the noise is diagonal with elements given by

$$C_{ii}^N = \frac{1}{\sigma_i^2} \quad , \qquad (7)$$

where σ_i is the variance of the measured visibilities. For a given set of n measured visibilities, one can test any theory, or set of $\{C_\ell\}$, by constructing the likelihood function (for complex visibilities)

$$\mathcal{L}\left(\{C_\ell\}\right) = \frac{1}{\pi^n \det C} \exp\left[-V^*(\mathbf{u}_i) C_{ij}^{-1} V(\mathbf{u}_j)\right] \quad , \qquad (8)$$

where $C_{ij} = C_{ij}^V + C_{ij}^N$ is the correlation matrix of visibilities at $\mathbf{u}_i$ and $\mathbf{u}_j$ (Hobson, Lasenby & Jones 1995).

4.1. Joint Confidence Intervals

Invoking Bayes' theorem and assuming a uniform prior for the amplitude of the fluctuations, we can determine the probability that the correct result is contained in an interval I,

$$P(I) = \frac{\int_I \mathcal{L}(z)dz}{\int_0^\infty \mathcal{L}(z)dz} \quad . \qquad (9)$$

The confidence interval corresponding to a probability P_0 is given by the I_0 such that $P(I_0) = P_0$ and $\mathcal{L}[z \in I_0] \geq \mathcal{L}[z \notin I_0]$. If the fields are entirely independent, the joint likelihood for the combination of the data sets to be described by a given model is simply equal to the product of the likelihoods for the individual

data sets,

$$\mathcal{L}(z) = \prod_i \mathcal{L}_i(z) \quad . \tag{10}$$

Combining the diagonal window functions corresponding to each visibility weighted by the noise, we can construct an effective diagonal window function to determine where the experiment is most sensitive;

$$\bar{W}_\ell = \sum_i \frac{W_{ii}(\ell) w_i}{\sum_\ell \frac{W_{ii}(\ell)}{\ell} \sum_i w_i} \quad , \tag{11}$$

where $w_i = 1/\sigma_i^2$. With this normalization,

$$\sum_\ell \frac{\bar{W}_\ell}{\ell} = 1 \quad . \tag{12}$$

Using the data weighted window function, we can determine the effective multipole of the experiment assuming the power spectrum is flat;

$$\ell_{eff} = \sum_\ell \bar{W}_\ell \quad . \tag{13}$$

4.2. Binning

The data sets for each of our fields contain on the order of $N = 10^5$ visibilities. The inversion of the covariance matrix required for the analysis is a $N^{2.8}$ process (Press et al. 1996). As discussed in Hobson, Lasenby & Jones (1995), considerable compression of the data is necessary if the analysis is to be completed in a reasonable amount of computing time. We divide the u-v plane into a grid of cells; all the visibilities within a cell are combined, weighted by the reciprocal of their estimated noise variance;

$$V_\alpha = \frac{\sum\limits_{i\in\alpha} \frac{V_i}{\sigma_i^2}}{\sum\limits_{i\in\alpha} \frac{1}{\sigma_i^2}} \quad . \tag{14}$$

We determine noise weighted u-v positions just as we have determined the values for the visibilities;

$$u_\alpha, v_\alpha = \frac{\sum\limits_{i\in\alpha} \frac{u_i}{\sigma_i^2}}{\sum\limits_{i\in\alpha} \frac{1}{\sigma_i^2}}, \frac{\sum\limits_{i\in\alpha} \frac{v_i}{\sigma_i^2}}{\sum\limits_{i\in\alpha} \frac{1}{\sigma_i^2}} \quad . \tag{15}$$

The sampling theorem tells us that the Fourier transform of the sky is completely specified by a sampling of the u-v plane on a regular grid with $\Delta u, \Delta v < 1/2\theta_p$ where θ_p is the angular radius of the primary beam. Because our final u-v points do not form a regular grid, it is possible that we would have to decrease the size of a our grid by a factor of two to strictly satisfy this criterion. Following Hobson, Lasenby & Jones (1995), we define the extent of the beam as the point at which the beam falls to 1% of its peak value, $\theta_p = 7.45'$. We determine that the u-v plane must be sampled more densely than $\Delta u, \Delta v = 230$. In practice, this is simple to achieve and we sample the u-v plane at intervals of $\Delta u, \Delta v = 60$ in the analysis presented in this paper. This compresses the number of u-v points to ~ 200 for each of the data sets.

4.3. Calibration

The likelihood analysis code has been checked by the analysis of simulated data sets. We took a data file from one of our observations, removed the visibilities, and replaced them with Gaussian distributed noise with the same weights as the original data. To this we added the Fourier transform of a realization of CMB anisotropy with flat band power that had been modulated with the measured BIMA primary beam. We produced 100 such data sets each with independent CMB and noise realizations. The simulated data were then analyzed in exactly the same way as the real data treating each data set as an independent (uncorrelated) observation. For an input flat-band power with $Q_{flat} = 30\,\mu$K, we found that the likelihood peaked at $Q_{flat} = 31\,\mu$K with values $29 - 33\,\mu$K and $27 - 35\,\mu$K allowed at 68% and 95% confidence. We interpret this as a demonstration that the analysis code is correctly calibrated.

5. Results

In this section, we use the method that we have described above to determine the relative likelihoods that the observed fields are described by a model for the CMB fluctuations with flat band power Q_{flat}.

Before proceeding, we discuss the effect of subtracting the known point sources on the anisotropy results. Three of the observed fields are known to have significant point source contamination. In Section 3.1, we discussed the determination of the source fluxes and positions. For the three contaminated fields, we subtract the Fourier transform of the point source model from the raw visibility data. In Figure 1, we plot the results of the likelihood analysis for the field PC1643+46 before and after the subtraction of the three detected point sources. The results are normal-

ized to unity likelihood for the case of no anisotropy signal. We have performed the same analysis with the point source fluxes found when the positions of the sources are fixed to the results of Jones et al. (1997). The results are essentially identical; the most likely value for Q_{flat} is again zero. In all further analysis, we use the point source fluxes and positions found from the fits to the OVRO and BIMA data. In Table 5, we show the results for Q_{flat} for the analysis of the three contaminated fields before point source subtraction. It is clear that neglecting to subtract the known point sources can lead to an erroneous detection of anisotropy.

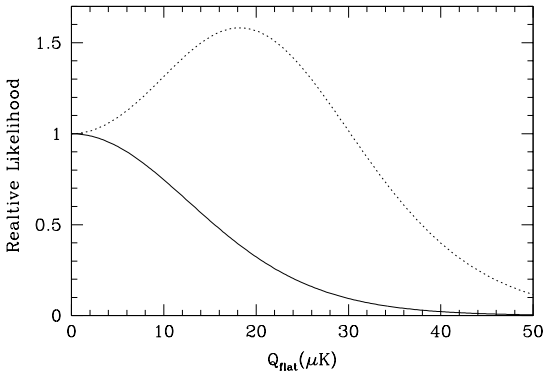

Fig. 1.— The relative likelihood that the observed signal in the PC1643+46 field is described by flat band power with amplitude Q_{flat}. The dotted line corresponds to an analysis ignoring the measured point sources and the the solid line is the result when the measured point source fluxes are subtracted from the visibility data.

In Figures 2 and 3, we plot the relative likelihood for each of the observed fields, where we have subtracted the detected point sources listed in Table 2. In Table 6, we list the 68% and 95% confidence intervals in Q_{flat} for each of the observed fields. The fields are independent and we can apply eqn. 10 to determine the joint likelihood for the combination of fields. The relative likelihoods of the joint fits are plotted in Figure 4. In Table 6, we also list the confidence intervals in Q_{flat} found from the joint fits. Because of the different array configurations and declinations of the sources, the window function for each observation is slightly different. We have used eqn. 11 to determine effective diagonal window functions corresponding to the 1997, 1998, and combination of the 1997 and 1998 data. These window functions are plotted as a function of multipole in Figure 5. Finally, we have used eqn. 13 to determine the effective multipole number, $\ell_{eff} \sim 5470$, of the results quoted here.

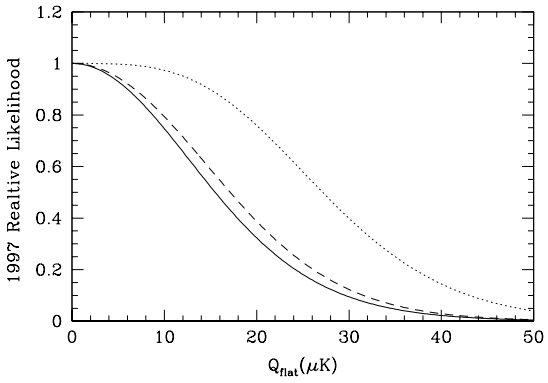

Fig. 2.— The relative likelihood that the observed signal in each of the 1997 data sets is described by flat band power with amplitude Q_{flat}. The solid, dashed, and dotted lines are for the fields PC 1643+46, PSS 0030+17, and VLA 1312+32 respectively.

One is immediately struck by the fact that the joint likelihood for all the data, shown in Figure 4, peaks at $Q_{flat} > 0$. However, this result has fairly low significance. Each of the individual fields are consistent with no signal on the sky at 95% confidence and the confidence of a non-zero Q_{flat} for the joint likelihood is only 44%.

After point source subtraction, none of the fields observed in 1997 produce a non-zero anisotropy signal. This is further evidence that the PC1643+46 and VLA1312+32 data are inconsistent with the presense of massive galaxy clusters in these fields as has been demonstrated by Holzapfel et al. (1999). There is also no evidence for a distant cluster in the PSS0030+17 field. From Table 6, we can see that including the 1997 data in the joint likelihood only reduces the limits on Q_{flat}.

5.1. Limits on Point Source Contamination

All of the excess power is found in the two fields which have the poorest limits on point source contamination of any of the seven fields. It is possible that point source contamination contributes to the signal in these fields. If the observed power is dominated by Poisson distributed point sources, we expect to find

Results Before Point Source Subtraction

	$Q_{flat}\,(\mu\mathrm{K})$		
Field	Most Likely	68%	95%
HDF 1236+62	4.8	$0.0 - 17.8$	$0.0 - 33.2$
PSS 0030+17	11.8	$0.0 - 31.6$	$0.0 - 61.8$
PC 1643+46	18.2	$4.8 - 29.0$	$0.0 - 42.2$

Table 5: Q_{flat} results before subtraction of known point sources. Compare with Table 6 to see the results after point source removal.

Most Likely Q_{flat} and Confidence Intervals

	$Q_{flat}(\mu\mathrm{K})$		
Field	Most likely	68%	95%
BF 0028+28	0.0	$0.0 - 8.5$	$0.0 - 17.5$
HDF 1236+62	0.0	$0.0 - 13.0$	$0.0 - 26.6$
BF 1821+59	18.6	$8.8 - 28.8$	$0.0 - 37.8$
BF 0658+55	19.0	$8.4 - 30.4$	$0.0 - 40.6$
Combined 1998 fields	8.8	$2.4 - 12.8$	$0.0 - 17.4$
PC 1643+46	0.0	$0.0 - 13.1$	$0.0 - 26.6$
VLA 1312+32	0.0	$0.0 - 20.5$	$0.0 - 38.0$
PSS 0030+17	0.0	$0.0 - 14.4$	$0.0 - 29.2$
Combined 1997 fields	0.0	$0.0 - 8.9$	$0.0 - 17.4$
All fields	5.6	$0.0 - 9.6$	$0.0 - 14.1$

Table 6: Results of the Bayesian analysis for each of the observed fields. Column 2 gives the most likely value for band power amplitude Q_{flat}. Columns 3 & 4 give the 68% and 95% confidence intervals.

$Q_{flat} \propto \ell$. We have verified this scaling by the analysis of both real and simulated data with significant point source emission. If this scaling was observed in these data sets, it would be a "smoking gun" for point source contamination.

Two of the fields we have observed, BF0658+55 and BF1821+59, yield significant detections of power on short baselines. The flat-band power in these fields, determined from a joint analysis of the $0.63 - 1.2\,\mathrm{k}\lambda$ data, is found to be $Q_{flat} = 18.9 \pm 7.2\,\mu\mathrm{K}$ at 68% confidence. To determine if this signal is due to point source contamination, we have reanalyzed the data assuming $Q = Q_0(\ell/\ell_0)$ rather than flat-band power. The effective multipole ℓ_0, to which Q_0 is referred, is chosen so that $Q_0 = Q_{flat}$ when both analyses are applied to the $0.63 - 1.2\,\mathrm{k}\lambda$ data. We have determined Q_0 for several fields with known point sources and find that, for the long baselines $(1.2 - 6.0\,\mathrm{k}\lambda)$, the value of Q_0 is identical to that found from the short baselines $(0.63 - 1.2\,\mathrm{k}\lambda)$ used in the anisotropy analysis. Applying this analysis to the combined long baseline data for the fields BF0658+55 and BF1821+59, we find no evidence for point source emission and constrain $Q_0 < 8.8\,\mu\mathrm{K}$ and $Q_0 < 15.8\,\mu\mathrm{K}$ at 68% and 95% confidence. Therefore, we conclude with 95% confidence that Poisson distributed point sources cannot be responsible for excess power found in the analysis of the short baseline data. However, if the signal is produced by several weak clustered point sources, such as in the PC1643+46 field, the scaling $Q_{flat} \propto \ell$ is not observed in either the real or simulated data. Therefore, weak clustered sources could be responsible for the observed signal.

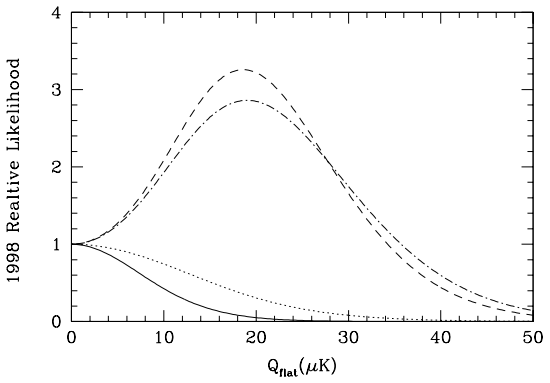

Fig. 3.— The relative likelihood that the observed signal in each of the 1998 data sets is described by flat band power with amplitude Q_{flat}. The solid, dashed, dotted, and dot-dashed lines are for the BF 0028+28, HDF 1236+62, BF 1821+59, and BF 0658+55 data respectively.

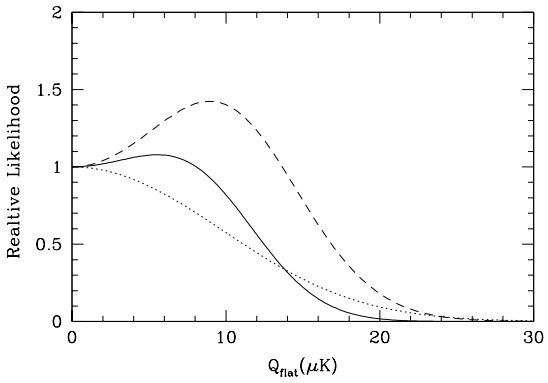

Fig. 4.— The relative joint likelihood that the data from each year is described by flat band power with amplitude Q_{flat}. The dotted, dashed, and solid lines correspond to the 1997, 1998, and combination of 1997 & 1998 data respectively.

6. Expected Signals

To interpret our results, it is informative to consider the level of the expected signals. In this section, we give our best estimates of the expected contributions from primary and secondary CMB anisotropies and foreground sources to the observed Q_{flat}. These results are compiled in Table 7.

6.1. Primary Anisotropies

We have convolved model CMB anisotropy power spectra with the window function of the experiment to determine the inferred flat band power signal,

$$Q_{flat}^2 = \left(\frac{5}{24\pi}\right) \sum_{\ell} C_\ell \ell \bar{W}_l d\ell \quad . \tag{16}$$

The CMB power spectra were generated using the CMBFAST code (Seljak & Zaldarriaga 1996). The expected signal for this experiment is largely determined by the total energy density of the universe, Ω_0. We have calculated Q_{flat} for a range of values for Ω_0 while keeping the baryon density $\Omega_B = 0.05$ and the Hubble constant $h = 0.65$ constant. For these observations, the majority of the signal comes from the small region of overlap between the BIMA array diagonal window function and the damping tail of the CMB. For total energy density $\Omega_0 = 1.0$ and 0.3, we expect primary anisotropy signals of $Q_{flat} = 1.1$ and $5.8\,\mu$K respectively.

6.2. Secondary Anisotropies

Sometime after recombination at redshift $z \sim 1100$, the universe was reionized. We know that this ionization was essentially complete by redshift $z \sim 5$ because spectra of distant quasars do not show a continuum of absorption by neutral hydrogen (Gunn & Peterson 1965). The interaction of the CMB with the reionized universe leads to secondary anisotropies. There are three types of secondary anisotropies which are expected to make significant contributions on arcminute scales: the Vishniac effect; inhomogeneous reionization; and the SZ effect.

The Vishniac effect is a "second order" Doppler shift which produces CMB temperature anisotropy by the fact that the large scale velocity field is modulated by small-scale variations in baryon density (Vishniac 1987; Ostriker & Vishniac 1986). While the other secondary anisotropies discussed in this section require variations in ionization, the Vishniac effect acts in a universe that is uniformly ionized. Hu & White (1996) have determined the size of the effect for a range of reionization histories in the context of a critical CDM model. For reionization epochs $z_r = 5$ and 100, they find signals of amplitude $Q_{flat} \sim 1.7$ and $3.6\,\mu$K which peak at multipole moments $\ell \sim 5000$ and 10000, respectively.

Inhomogeneous reionization will imprint Doppler shifts, due to the velocities of the reionized regions, on the Compton scattered CMB photons (Kaiser 1984).

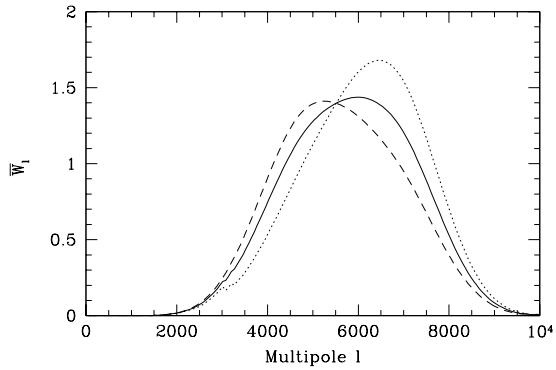

Fig. 5.— The "data weighted" window functions $\bar{W}_\ell$. The dotted, dashed and solid lines correspond to the 1997, 1998, and combination of 1997 & 1998 data respectively.

The effect of inhomogeneous reionization has been studied most recently by Gruzinov & Hu (1998) and Knox, Scoccimarro, & Dodelson (1998). There are considerable uncertainties in the details of the generation of ionized regions. To obtain an accurate result, the correlation of the ionizing regions must be taken into account. For universes that reionizes at $z_i = 26$ and 31 , Knox, Scoccimarro, & Dodelson (1998) find a flat-band temperature anisotropy of $Q_{flat} \sim 1.8$ and $2.5\,\mu$K at $\ell = 5500$. Observation of this signal would provide useful constraints on what are presently highly speculative reionization scenarios.

The majority of luminous matter in massive clusters of galaxies is observed to exist in the form of ionized gas which has been heated by gravitational infall. This hot gas can present a considerable inverse Compton scattering cross section to CMB photons. The resulting spectral distortion in the direction of a cluster of galaxies is known as the Sunyaev-Zel'dovich effect (SZE) (Sunyaev & Zel'dovich 1972). The change in RJ CMB temperature in the direction of a massive cluster can be as large as 1 mK. For a recent review see Birkinshaw (1999) and the references within. Several authors have computed the expected CMB anisotropy power spectrum due to the SZE in clusters of galaxies (Atrio-Barandela & Mücket 1999; Komatsu & Kitayama 1999; Holder & Carlstrom 1999). The treatments differ in the range of cosmological models considered and the models for the cluster evolution. One general conclusion is that, at the small angular scales relevant for this experiment, the majority of the signal is due to distant less massive clusters and removing either the bright SZE or x-ray sources does not appreciably change the results. In general, the results depend sensitively on the assumed cosmology and cluster evolution model. For example, Holder & Carlstrom (1999) find that at $\ell \sim 5000$, $Q_{flat} = 1.3 - 8.0\,\mu$K for the range of models they consider.

6.3. Undetected Radio Point Sources

In Section 3.1, we described our mechanism for measuring and removing point sources. As seen in Tables 3 and 4, the flux sensitivity of the data with baselines longer than $2.4\,\mathrm{k}\lambda$ is comparable to that of the $0.63 - 1.2\,\mathrm{k}\lambda$ data. Although we see no evidence for additional point sources, we cannot reliably constrain the presence of point sources below 3σ in the high resolution maps which corresponds to a flux of $\sim 300 - 500\,\mu$Jy.

We have attempted to quantify the expected signals from point sources both analytically and through simulations. The integrated source counts with fluxes less than S_{cut} have been measured at 8.4 GHz by Partridge et al. (1997). We take their result and scale it to the BIMA observing frequency of 28.5 GHz by using the average measured radio power law index ($\alpha = 0.77$) from Cooray et al. (1998). The number density of sources then becomes

$$N(>S_{cut}) = \frac{20}{\mathrm{arcmin}^2}\left(\frac{\nu}{8.4\,\mathrm{GHz}}\right)^{-\beta\alpha}\left(\frac{S_{cut}}{\mu\mathrm{Jy}}\right)^{-\beta} \quad , \tag{17}$$

where $\beta = 1.2$. We follow the treatment of Scott & White (1999) and estimate the contribution to the power spectrum to be

$$C_\ell \sim \frac{\beta}{\left(\frac{dB}{dT}\right)^2(2-\beta)} N(>S_{cut}) S_{cut}^2 \quad , \tag{18}$$

where S_{cut} is the minimum source flux which we can remove from our maps. Using equation 16, we can then determine the contribution of point sources to Q_{flat}. For the maximum residual source flux, $S_{cut} = 400\,\mu$Jy, we find $Q_{flat} = 6.6\,\mu$K.

In order to test this approximation, we simulated distributions of point sources on the sky. For each simulated sky, we generated a sample of point sources with fluxes less than $S_{cut} = 400\,\mu$Jy drawn from the dN/dS distribution given in Partridge et al. (1997).

The sources are placed at random in the field. These model skies are then Fourier transformed and added to a unique manifestation of visibilities consistent with the weights of one of our complete data sets. The simulations are then analyzed exactly as the real data. When we analyzed 100 manifestations of the sky generated in this way, we found $Q_{flat} = 4.8^{+2.0}_{-2.8}\,\mu$K at 68% confidence. So, the source simulations and analytic approximation predict similar signals which, interestingly, are of the same order as the most likely signal in the data.

However, as described in Section 1, the observed fields were selected to be free of bright radio sources at 1.4 GHz. If the sources have a falling spectrum, we will have selected fields with significantly lower than typical point source confusion at 28.5 GHz. Also, for the fields PC1643+46 and VLA1312+32, additional OVRO observations were used to remove point sources down to $\sim 200\mu$Jy. Therefore, the estimates for point source contamination presented here are upper limits to the expected signal in our data.

6.4. Anomalous Dust Emission

Recently, anomalous foreground emission at microwave frequencies has been observed which is found to be strongly correlated with IRAS 100 μm maps (Leitch et al. 1997; de Oliveira-Costa et al. 1997). It has been proposed that this emission may be due to either free-free emission (Kogut et al. 1996) or dipole emission from rapidly spinning dust grains (Draine & Lazarian 1997). From a compilation of experimental results, Kogut (1999) has determined a scaling between emission in the IRAS 100 μm band and at microwave frequencies. At 28.5 GHz, we expect this scaling to be approximately $17\,\mu\mathrm{K}/(\mathrm{MJy\,sr^{-1}})$. As mentioned in Section 2.2, we selected fields to have minimal 100 μm emission and contrast. We have determined the *rms* 100 μm flux for each of our observed fields. The resolution of the IRAS maps is 1.5′ and therefore well matched to the angular scale on which the BIMA experiment is sensitive. The observed fields are found to have a range of *rms* fluctuations $\Delta I_{100\mu} = 0.04 - 0.09\,\mathrm{MJy\,sr^{-1}}$. Therefore, we expect a *rms* temperature signal from this foreground of $\Delta T < 1.7\,\mu$K, which corresponds to $Q_{flat} < 1.1\,\mu$K.

6.5. Systematic Errors

The detected signals could also be the result of subtle systematic errors. The observations presented here represent the deepest images we have made of fields without strong SZE decrements due to known galaxy clusters and therefore could be subject to undiscovered systematic errors. Without success, we have extensively searched for a non-astronomical explanation of the observed excess power. The results are found to be constant across the observing frequency band, independent of baseline or telescope, reproducible from day to day, and uncorrelated with the position of the sun or moon during our observations. If this work is subject to systematic errors, deeper observations will be necessary in order for them to manifest themselves in a significant manner.

Expected Contributions to Q_{flat}

Signal	$Q_{flat}(\mu\mathrm{K})$
Primary Anisotropy	$1.1 - 5.8$
Vishniac Effect	$1.7 - 3.6$
Inhomogeneous Reionization	$1.8 - 2.5$
Sunyaev-Zel'dovich Effect	$1.3 - 8.0$
Point Sources	< 6.6
Spinning Dust/Free-Free	< 1.1
Total	$3.0 - 12.7$

Table 7: Expected flat-band power due to primary anisotropy, secondary anisotropy, and foreground confusion.

7. Comparison with Previous Work

There here have been many previous searches for anisotropy in the CMB at arcminute scales. The results of this earlier work have been expressed in several different ways. Until recently, it was common for experimenters to quote limits on CMB anisotropies with a Gaussian autocorrelation function (GACF)

$$C(\theta) = C_0\, exp\left(-\frac{\theta^2}{2\theta_c^2}\right) \quad , \tag{19}$$

where θ_c is the coherence angle and $\sqrt{C_0}$ is the variance of the CMB. Given the diagonal elements of the average window function, it is simple to convert between flat band power and GACF results (Bond 1995). Here we express our results in terms of limits on temperature anisotropy with a GACF in order to facilitate comparison with the results of other experiments. At the scale of maximum sensitivity $\theta_c = 0.9'$, our 68% and 95% confidence limits on $\sqrt{C_0}/T_{cmb}$ are 6.5×10^{-6} and 9.6×10^{-6} respectively.

In previous work, both single dish and interferometric techniques have been used to perform sensitive searches for CMB anisotropies on arcminute scales. In Table 8, we list the frequency, sky coverage, coherence angle corresponding to maximum sensitivity, and 95% confidence limits on variance and flat-band power for each of the most sensitive experiments and compare them with our results.

Operating at a frequency of 20 GHz, the Owens Valley Radio Observatory (OVRO) 40 m dish has been used to measure sensitive differences between beams of $\sim 1.8'$ *fwhm* separated by $\sim 7'$ (Readhead et al. 1989). They express their results in terms of limits on fluctuations with a GACF. At the coherence angle for which the experiment is maximally sensitive, $\theta_c = 2.6'$, they constrain $\sqrt{C_0}/T_{cmb} < 1.7 \times 10^{-5}$ at 95% confidence. The effective total sky coverage of the experiment is estimated to be $\sim 60\,\mathrm{arcmin}^2$. More recently, the OVRO Ring experiment used the OVRO 40 m telescope to make a significant detection of anisotropy in a field near the North Celestial Pole (Myers et al. 1993). These results are inconsistent with the earlier work at OVRO and are likely to be the result of foreground contamination.

The SuZIE experiment is a drift scanning bolometer array. Fielded at the CalTech Submillimeter Observatory (CSO), it was used to map $\sim 213\,\mathrm{arcmin}^2$ of blank sky at its operating frequency of 142 GHz (Church et al. 1997). Unlike the other experiments discussed here, radio point sources are not a significant source of confusion for SuZIE. They also express their results in terms of limits on fluctuations with a GACF. At the coherence angle of maximum sensitivity, $\theta_c = 1.1'$, they find $\sqrt{C_0}/T_{cmb} < 2.1 \times 10^{-5}$ at 95% confidence.

Interferometers have also proved to be very effective for making sensitive maps of the sky with arcminute resolution. Using the Very Large Array (VLA) at 8.4 GHz, Partridge et al. (1997) obtained an extremely deep 21 arcmin^2 image of the sky. On the scale at which the experiment is most sensitive (resolution $\sim 60''$) they find $\Delta T/T_{cmb} < 2.0 \times 10^{-5}$ at 95% confidence which corresponds to $Q_{flat} < 35.2\,\mu$K. In order to achieve this limit, they are forced to subtract a statistical estimate of the image variance due to point sources. Because we do not have exact knowledge of the window function of the VLA observations, we cannot determine the response of their system to CMB anisotropy with a GACF.

A group working with the Australian Telescope Compact Array (ATCA) has recently produced what were, previous to this work, the lowest limits on arcminute scale CMB anisotropies (Subrahmanyan et al. 1998). They observed at a lower frequency of 8.45 GHz, but the larger size of the ATCA dishes compensates to make the window function of the ATCA and BIMA experiments similar. Using a single deep pointing of their array ($\sim 28\,\mathrm{arcmin}^2$), they constrained $Q_{flat} < 23.6\,\mu$K at 95% confidence on an angular scale corresponding to $\ell_{eff} \sim 4600$. They also express their results in terms of anisotropy with GACF. At the coherence angle for which the experiment is maximally sensitive, $\theta_c = 1.0'$, they find $\sqrt{C_0}/T_{cmb} < 1.6 \times 10^{-5}$ at 95% confidence.

8. Conclusion

We have used the BIMA array in a compact configuration at 28.5 GHz to search for CMB anisotropy in seven independent fields. With these observations, we have placed the lowest limits on arcminute scale CMB anisotropies to date. These results are determined from $\sim 240\,\mathrm{arcmin}^2$ of sky; this is the largest sky coverage of any of the arcminute scale anisotropy experiments. In the context of an assumed flat band power model for the CMB power spectrum, we find $Q_{flat} = 5.6^{+3.0}_{-5.6}\,\mu$K at 68.3% confidence and $Q_{flat} < 14.1\,\mu$K at 95.4% confidence with sensitivity centered about harmonic multipole $\ell_{eff} = 5470$. This result includes the three fields observed in 1997 which were previously suspected to contain possible distant clusters. None of these fields contribute to the observed excess power.

A detection of excess power is not surprising when one considers the level of the signals expected from secondary CMB anisotropies and foreground emission. We have ruled out Poisson distributed point sources as the cause of the detected excess power at greater than 95% confidence, although, faint clustered sources could still be responsible. It is possible that we have detected some combination of secondary CMB anisotropies and faint radio point sources, however, the confidence of the detection is only 44%.

In the coming year, we plan to expand our observations to include greater sky coverage and deep searches for point sources. Future observations with broader correlated bandwidth could reach sensitivities an order of magnitude higher than presented here. With proper characterization of foregrounds, these observations may be able to place interesting

Comparison With Previous Work

Experiment	ν (GHz)	Ω_{sky} (arcmin^2)	θ_c (arcmin)	95% Confidence Limits $\sqrt{C_0}/T_{cmb}$	Q_{flat}
SuZIE	142	213	1.1	2.1×10^{-5}	–
OVRO 40 m	20	~ 60	2.6	1.7×10^{-5}	–
VLA	8.4	20	~ 1.0	–	35.2
ATCA	8.4	28	1.0	1.6×10^{-5}	23.6
BIMA	28.5	240	0.9	9.6×10^{-6}	14.1

Table 8: Frequency, sky coverage, coherence angle, and 95% confidence limits on the variance and flat-band power from previous work and the BIMA results.

constraints on models for the reionization of the universe.

Many thanks to the staff of the BIMA and OVRO observatories for their contributions to this project. In particular, a high five to Dick Plambeck, Rick Forster, and John Lugten for their help with the BIMA observations. We would also like to thank Cheryl Alexander for her help in the construction of the cm-wave receivers. Thanks to Asantha Cooray and Sandy Patel for help with the OVRO and BIMA observations. Radio Astronomy with the OVRO millimeter array is supported by NSF grant AST 96-13717. The BIMA millimeter array is supported by NSF grant AST 96-13998. JEC acknowledges support from a NSF-YI grant and the David and Lucile Packard Foundation. EDR and LG acknowledge support from NASA GSRP fellowships. This work is supported in part by NASA LTSA grant number NAG5-7986. Finally, we would like to acknowledge informed discussions with Martin White and Ravi Subrahmanyan.

REFERENCES

Atrio-Barandela, F. & Mücket, J. P. 1999, ApJ, 515, 465.

Birkinshaw, M. 1999, *Physics Reports*, 310, 97.

Bond, R. 1995, *Astro. Lett. and Communications*, 1995, 32, 63.

Carlstrom, J. E., Joy, M., & Grego, L. 1996, ApJ, 456, L75.

Carlstrom, J. E., Joy, M., Grego, L., Reese, E. D., Patel, S., Holder, G., Cooray A., & Holzapfel W. L. 1999, Physical Scripta, 60, in press, astro-ph/9905255

Church, S. E., Ganga, K. M., Holzapfel, W. L., Ade, P. A. R., Mauskopf, P. D., Wilbanks, T. M., & Lange A. E. 1997, ApJ, 484, 523.

Condon, J. J., Cotton, W. D., Greisen, E. W., Yin, Q. F., Perley, R. A. Taylor, G. B. & Broderick, J. J. 1998, AJ, 115, 1693.

Cooray, A. R., Grego, L., Holzapfel, W. L., Joy, M., & Carlstrom, J. E. 1998, AJ, 115, 1388.

Djorgovski, G. 1997, private Communication.

Draine, B. T. & Lazarian, A. 1998, ApJ, 494, 19.

Grego, L. 1998, Ph. D. thesis, Caltech.

Gruzinov, A. & Hu, W. 1998, ApJ, 508, 435.

Gunn, J. E. & Peterson, B. A. 1965, ApJ, 142, 1633.

Haiman, Z. & Knox, L. 1999, astro-ph/9902311.

Hobson, M. P., Lasenby, A. N., & Jones, M. 1995, MNRAS, 275, 863.

Hobson, M. P. & Mageuijo, J. 1996, MNRAS, 283, 1133.

Holder, G. & Carlstrom, J. E. 1999, astro-ph/9904220.

Holzapfel, W. L., Carlstrom, J. E., Joy, M., Grego, L., & Reese, E. D. 1999, ApJ, submitted.

Hu, W. & White, M., 1996, A&A, 315, 33.

Hu, W. & White, M., 1997, ApJ, 479, 568.

Jones, M. E., Saunders, R., Baker, J. C., Cotter, G., Edge, A., Grainge, K. Hayes, T., Lasenby, A., Pooley, G., & Röttgering, H. 1997, ApJ, 479, L1.

Kaiser, N. 1984, ApJ, 282, 374.

Kogut, A., Banday, A. J., Bennett, C. L., Gorski, K. M., Hinshaw, G., Smoot, G. F., & Wright, E. I. 1996, ApJ, 464, L5.

Kogut, A. 1999, astro-ph/9902307.

Komatsu, E. & Kitayama, T. 1999, astro-ph/9908087.

Knox, A., Scoccimarro, R., & Dodelson, S. 1998, Phys. Rev. Letters, 81, 2004.

Leitch, E. M., Readhead, A. C. S., Pearson, T. J. & Myers, S. T. 1997, ApJ, 486, L2.

Martin, H. M. & Partridge, R. B. 1988, ApJ, 324, 794.

Myers, S. T., Readhead, A. C. S., & Lawerence, C. R. 1993, ApJ, 405, 8.

de Oliveira-Costa, A., Kogut, A., Devlin, M. J., Netterfield, C. B., Page, L. A., & Wollack, E. J. 1997, ApJ, 482, L17.

Ostriker, J. P. & Vishniac, E. T. 1986, ApJ, 306, L51.

Partridge, R. B., Richards, E. A., Fomalont, E. B., Kellerman, K. I., & Windhorst, R. A. 1997, ApJ, 438, 38.

Pospieszalski, M. W., Lakatosh, W. J., Nguyen, L. D., Lui, T., Le, M., Thompson, M. A., & Delaney, M. J. 1995, Microwave Symposium Digest, IEEE MTT-S International, 3, 1121.

Press, W. H., Teukolsky, S. A., Vetterling, W. T., & Flannery, B. P. 1996, Numerical Recipes: the art of scientific computing, 2nd. edition, Cambridge University Press.

Readhead, A. C. S., Lawerence, C. R., Myers, S. T., Sargent, W. L. W., Hardebeck, H. E., & Moffet, A. T. 1989, ApJ, 346, 566.

Richards, E. A., Partridge, R. B., Fomalont, E. B., Kellerman, K. I., & Windhorst, R. A. 1997, ApJ, 483, 38.

Richards, E. A., Kellerman, K. I., Fomalont, E. B., Windhorst, R. A., & Partridge, R. B. 1997, AJ, 116, 1039.

Seljak, U. & Zaldarriaga, M. 1996, ApJ, 469, 437.

Subrahmanyan, R., Ekers, R. D., Sinclair, M., & Silk, J. 1993, MNRAS, 263, 416.

Subrahmanyan, R., Ekers, R. D., Sinclair, M., & Silk, J. 1998, MNRAS, 298, 1189.

Sunyaev, R. A. & Zel'dovich, Ya. B. 1972, *Comments on Astrophysics and Space Science*, 4, 173.

White, R. L., Becker, R. H., Helfand, D. J. & Gregg, M. D. 1997, ApJ, 475, 479.

White, M., Carlstrom, J. E., Dragovan, M., & Holzapfel, W. L. 1999, ApJ, 514, 12.

Vishniac, E. T. 1987, ApJ, 322, 597.

This 2-column preprint was prepared with the AAS LaTeX macros v4.0.